



Initial Study on Metal Dusting Behavior of Fe–Cr and Fe–Ni–Cr Alloys Under a Simulated Blast Furnace Operating Condition

Tatsuya Murakami¹ · Thuan Dinh Nguyen¹ · Xuteng Xi¹ · Jianqiang Zhang¹

Received: 28 March 2023 / Revised: 13 July 2023 / Accepted: 24 July 2023 /

Published online: 5 August 2023

© The Author(s) 2023

Abstract

Blast furnace ironmaking produces a reducing and carburizing atmosphere in the blast furnace which may lead to metal dusting. However, there is limited research on metal dusting under this particular atmosphere. This paper investigated metal dusting behaviors of ferritic Fe-(10, 20, 25)Cr and austenitic Fe-20Cr-(20, 33)Ni, Fe-25Cr-20Ni (wt.%) alloys at 550 and 650 °C in an Ar-33CO-7H₂-7CO₂-2H₂O (vol.%) gas simulating a blast furnace operating condition. A relatively short reaction time, up to 100 h, was used to evaluate the initial stage of metal dusting of these alloys in the blast furnace gas condition. Severe metal dusting and coke deposition were observed at 550 °C, while no significant dusting but internal oxidation and carburization were observed at 650 °C. Higher Cr and Ni contents in the alloy lowered kinetics of metal dusting at 550 °C and of carburization at both temperatures. Austenitic alloys were more susceptible to metal dusting and coke deposition than ferritic alloys with the same Cr content at 550 °C. At 650 °C, however, ferritic alloys experienced higher extents of carburization and oxidation than austenitic alloys with the same Cr concentration. The effects of alloy composition and reaction temperature on metal dusting in this simulated blast furnace operating condition were discussed.

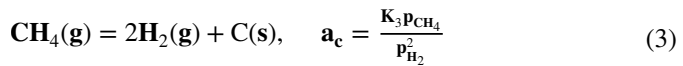
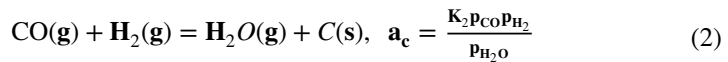
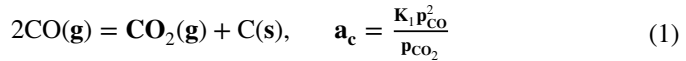
Keywords High temperature corrosion · Alloy · Carburization · Oxidation · Metal dusting

✉ Jianqiang Zhang
j.q.zhang@unsw.edu.au

¹ School of Materials Science and Engineering, University of New South Wales, Sydney, NSW 2052, Australia

Introduction

A highly carburizing gas (carbon activity, $a_C > 1$) with a relatively low oxygen partial pressure at elevated temperatures is widely acknowledged to cause metal dusting, where the surface of the bulk metal is disintegrated into powders or dusts containing carbon, carbides and metal particles. The gas carbon activity can be determined based on the Boudouard reaction, CO hydrogenation reaction, and methane decomposition reaction, respectively, as shown as follows:



where K is the equilibrium reaction constant, and p is the gas partial pressure. The carbon activity greater than unity is one of the requirements for metal dusting occurrence. Metal dusting has been a subject of research for decades, and the mechanisms have been proposed [1–4]. Equipment failures caused by metal dusting have been reported in industries, including heat exchangers for synthesis gas, gas heaters of direct reduction plants, platformer units in a refinery, direct reduction furnaces, reforming plants, etc. [5–7]. Such equipment failures could result in a huge loss of safety and productivity in industries, which requires fully understanding metal dusting in these processes.

A blast furnace used in steel industry is one of the facilities that has a carburizing environment at elevated temperatures. Figure 1 presents some experimental gas compositions of H_2 and CO obtained from total 274 previous studies, where the brighter the point is, the higher the number of this composition used. It should be mentioned that in this figure only H_2 and CO , as main gas components, were picked up, and only few of these 274 studies were listed in the references [1–4, 6, 8, 9]. The range of gas compositions in the blast furnace [10, 11] is also shown in this figure (as a rectangle square), illustrating that almost no existing work has been done in this particular gas composition range. In addition, the gas temperature in the blast furnace has been found to be in a broad range of 300–2200 °C [12–14], which contains a preferable temperature range for metal dusting (about 400 to 800 °C) [4–9]. This temperature range is located in the charging zone and top of preheating zone of the blast furnace where the gases have more chances in contact directly with the steel. Thus, the investigation of metal dusting behavior of materials in the blast furnace is necessary to prevent catastrophic failure due to metal dusting, if it occurs. Such a work has never been investigated before and no effort was made to compare these results to other studies in different dusting conditions.

To prevent metal dusting, it is required for the alloy to form a protective Cr-rich oxide layer on the surface to suppress inward carbon diffusion. Thus, chromium and

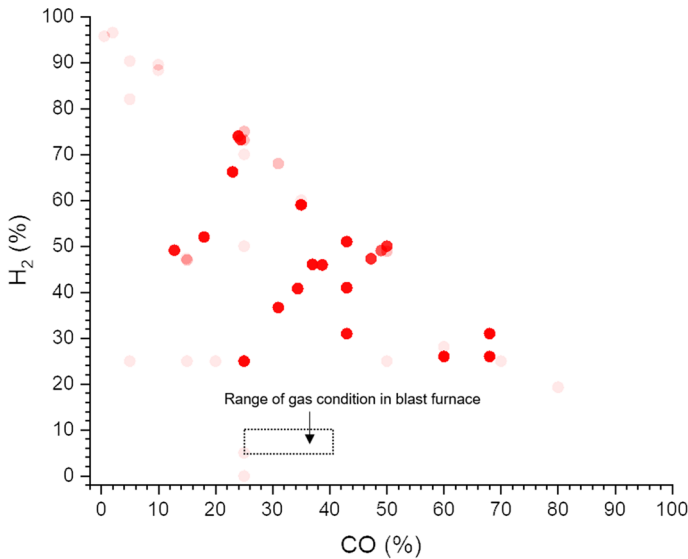


Fig. 1 Experimental gas conditions (CO and H₂) used in the previous studies (based on 274 experimental conditions) and the range of gas conditions obtained in a blast furnace. The brightness of marks is proportional to the number of gas conditions taken from these studies

nickel would be important alloying elements because the formation of Cr₂O₃ needs a critical amount of Cr in the alloy [5, 8, 9, 15] and the addition of Ni leads to a decrease in the carbon permeability of Fe–Ni alloys [5, 8, 16].

Therefore, this paper examined metal dusting behaviors of model Fe–Cr and Fe–Ni–Cr alloys in CO–H₂–CO₂–H₂O gases at 550 and 650 °C, simulating a blast furnace operation condition. A relatively short reaction time, up to 100 h, was used to evaluate the initial stage of metal dusting of these alloys in the blast furnace gas condition. The effects of alloy compositions and reaction temperature on metal dusting behaviors were studied.

Experimental Procedures

Six model alloys (Fe-10Cr, Fe-20Cr, Fe-25Cr, Fe-20Cr-20Ni, Fe-20Cr-33Ni, and Fe-25Cr-20Ni, all in wt.%) were prepared by arc melting pure metals in an Ar-5%H₂ gas atmosphere, using a tungsten electrode. The cast samples were then annealed in a flowing Ar-5%H₂ gas at 1050 °C for 70 h and cooled with the furnace to homogenize the samples. An analysis by X-ray diffraction (XRD) revealed that Fe-(10, 20, 25)Cr were ferritic, while Fe-20Cr-(20, 33)Ni and Fe-25Cr-20Ni were austenitic. Compositions of the alloys were confirmed by SEM–EDS analysis after annealing, showing only small deviations (± 0.3 wt. %) from the designed compositions. These alloys were designed to investigate Cr effect on both ferritic Fe–Cr and austenitic Fe-20Ni–Cr alloys, and also Ni effect on austenitic Fe-20Cr–Ni alloys.

Rectangular specimens were then prepared by cutting the button samples, and a hole near the edge of each specimen was drilled. The specimens were ground to a 1200 grit finish and further polished to a 3 μm finish, followed by electropolishing in an 18% HCl -82% H_2O solution at 4.0–4.5 V for 8–30 s to produce a deformation-free surface. Microstructure of each model alloy before a reaction revealed by electropolishing is shown in Fig. 2, showing that Fe-10Cr was mainly consisted of equiaxed grains with sizes of 100–500 μm , whereas all other alloys contained columnar grains with the widths ranging from 200 to 750 μm , and the lengths over several millimeters.

Specimens were hung inside a vertical silica tube reactor sitting inside a furnace for isothermal reactions at 550 and 650 $^\circ\text{C}$ in a flowing gas for up to 100 h. The reaction gas composition was controlled by mass flow controllers to be Ar-33 CO -7 H_2 -7 CO_2 -2 H_2O with a linear flow rate of 56 cm/min and 63 cm/min at 550 and 650 $^\circ\text{C}$, respectively. This gas composition was chosen based on the gas composition range in a blast furnace [10, 11]. The wet gases were generated by passing a mixture gas of CO , H_2 , and CO_2 through a water bath containing distilled water at a controlled temperature 29 $^\circ\text{C}$ [17]. A copper tubing from a thermostat to the reactor was heated to approximately 40 $^\circ\text{C}$ to prevent the condensation of water outside the thermostat.

Equilibrium oxygen partial pressure of the reaction gases, p_{O_2} , and a supersaturated gas carbon activity, a_c , are summarized in Table 1. The carbon activities were calculated in two ways where Reactions 1 and 2 are assumed to be dominant carburization reactions, respectively. The oxygen partial pressures were calculated using FactSage software [18]. Before reaction, a vertical furnace was moved to the upper part of the reactor tube during the period of heating, leaving specimens below the furnace region. When the furnace temperature reached the setting temperature, the

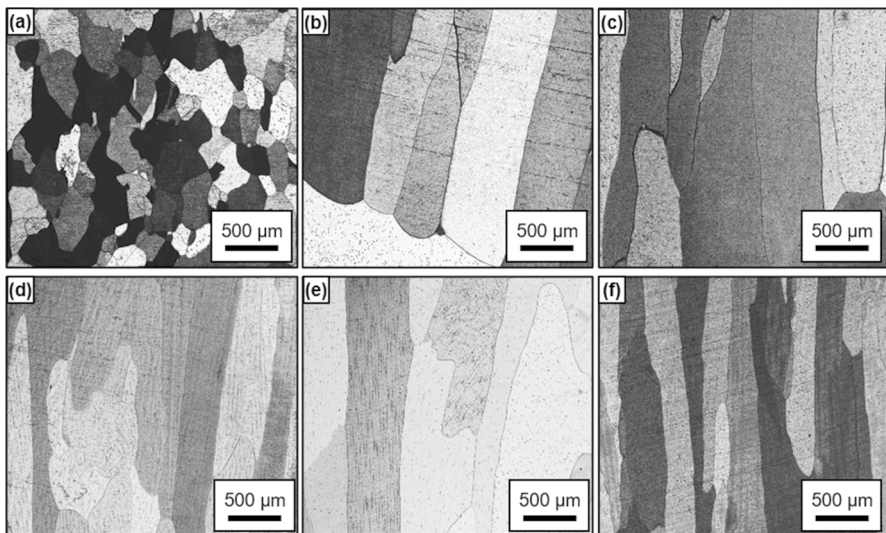


Fig. 2 Microstructures of model alloys revealed by electropolishing **a** Fe-10Cr; **b** Fe-20Cr; **c** Fe-25Cr; **d** Fe-20Cr-20Ni; **e** Fe-20Cr-33Ni; and **f** Fe-25Cr-20Ni

Table 1 Oxygen partial pressure and carbon activity of reaction gas (Ar-33CO-7H₂-7CO₂-2H₂O)

		Temperature (°C)	
		550	650
Oxygen partial pressure (atm)	p_{O_2}	1.8×10^{-26}	5.8×10^{-24}
Carbon activity	a_C		
the Hydrogeneration reaction		15.5	1.8
the Boudouard reaction		76.7	5.1

furnace was moved down, letting the specimens within the hot zone of the furnace to initiate reaction.

Specimens were weighed before and after reaction using a micro balance (Precisa 180A) with an accuracy of ± 0.01 mg. After that, the coke was removed by scrubbing with a soft bristle brush, and the cleaned specimens were re-weighed. As a result, alloy weight change and coking kinetics as a function of the exposure time were determined. The reaction products on the surface of alloys after reaction and removed coke deposits were analyzed by x-ray diffraction (XRD; Empyrean II) with a cobalt source. Cross sections of the reacted samples were analyzed using the following techniques—Optical microscopy (OM; Nikon Eclipse ME600); and scanning electron microscopy (SEM; FEI Nova NanoSEM 450) equipped with energy-dispersive X-ray spectroscopy (EDS; Bruker). Murakami's reagent (10 g KOH, 10 g K₃Fe(CN)₆, 100 ml H₂O) was used to etch cross-sectional samples to reveal the carbides. The values of pitting depth, internal oxide precipitation depth, carbide precipitation depth, volume fraction of internal oxide precipitates, and that of carbide precipitates were measured from optical micrographs using ImageJ software [19]. More than 10 different areas were measured to obtain average values of depths with the standard deviations.

Results

Reaction at 550 °C

Figure 3a and b shows alloy weight changes after removing coke and coke deposits obtained from the coke removal at 550 °C. Most of coke deposits after 100 h reaction at 550 °C were spalled during the exposure and sample handling process. Thus, Fig. 3b shows the weight of coke deposit only up to 20 h. A mass-loss was seen for all post-tested alloys after coke removal except for Fe-25Cr which exhibited a slight mass gain. The incubation time for the occurrence of mass loss was the shortest for Fe-10Cr. Fe-20Cr-20Ni showed the highest weight loss after 100 h reaction, while Fe-20Cr exhibited the lowest mass loss, excluding that of Fe-25Cr with a slight weight gain. In terms of coke deposits shown in Fig. 3b, Fe-10Cr, Fe-20Cr-(20, 33) Ni, and Fe-25Cr-20Ni exhibited higher weight of coke deposits than Fe-(20, 25)Cr, which is generally consistent with the results of the mass change in Fig. 3a.

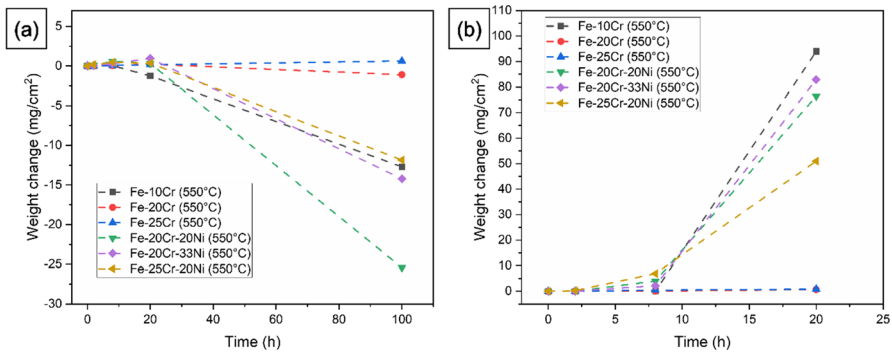


Fig. 3 Weight change kinetics ($\Delta W/A_0$, ΔW : weight change, A_0 : original surface area) at 550 °C **a** samples after removing coke; **b** coke deposits obtained from coke removal

Table 2 presents sample surface XRD results after coke removal after 100 h reaction at 550 °C. A matrix phase was always identified in all of model alloys, together with cementite, Cr_7C_3 , and FeCr_2O_4 . Graphite was found in all alloys but not Fe-25Cr, and Cr_2O_3 was identified in all alloys but not Fe-10Cr. Additionally, coke deposits collected from Fe-25Cr and Fe-20Cr-20Ni at 550 °C after 100 h reaction were analyzed using XRD and the results are shown in Table 3. A major phase was shown to be graphite, and cementite was also detected in both coke deposits. A matrix phase and FeCr_2O_4 were also identified in coke deposits collected from Fe-20Cr-20Ni. These identifications illustrated that Fe-25Cr and Fe-20Cr-20Ni had undergone metal dusting although Fe-25Cr kept weight gain after coke removal as shown in Fig. 3a. Furthermore, the detection of FeCr_2O_4 in coke deposits in Fe-20Cr-20Ni indicates the spinel oxide had been formed and removed from the surface.

Table 2 Sample surface XRD results after coke removal on the surface at 550 °C

Alloy	Phases
Fe-10Cr	Ferrite, Graphite, Fe_3C , Cr_7C_3 , FeCr_2O_4
Fe-20Cr	Ferrite, Graphite, Fe_3C , Cr_7C_3 , Cr_2O_3 , FeCr_2O_4
Fe-25Cr	Ferrite, Fe_3C , Cr_7C_3 , Cr_2O_3 , FeCr_2O_4
Fe-20Cr-20Ni	Austenite, Graphite, Fe_3C , Cr_7C_3 , Cr_2O_3 , FeCr_2O_4
Fe-20Cr-33Ni	Austenite, Graphite, Fe_3C , Cr_7C_3 , Cr_2O_3 , FeCr_2O_4
Fe-25Cr-20Ni	Austenite, Graphite, Fe_3C , Cr_7C_3 , Cr_2O_3 , FeCr_2O_4

Table 3 Reaction products in coke deposits at 550 °C after 100 h identified by XRD

Coke from	Reaction products
Fe-25Cr	Graphite, Fe_3C
Fe-20Cr-20Ni	Graphite, Austenite, FeCr_2O_4 , Fe_3C

Cross sections of post-tested alloys at 550 °C for 100 h were analyzed by optical microscopy, SEM with EDS, and the results are shown in Figs. 4, 5 and 6. For Fe-10Cr, surface attack performed more or less uniformly with intragranular and intergranular carbides formed near the alloy surface (Fig. 4a, b). Observation of BSE-SEM (Fig. 4c) revealed a thin coke scale on the surface containing graphite and fine iron-rich particles (Fig. 4c). Further EDS lines scan A-B through this coke layer (Fig. 4d) confirmed very high content of C in the coke layer with mainly Fe and very low content of Cr in the coke layer.

For Fe-20Cr alloy, after 100 h reaction, a wavelike surface was observed (Fig. 5a), indicating a nonuniform attack. There was a dark band underneath the surface which corresponds to the carburization zone. Higher magnification image (Fig. 5b) revealed a thin discontinuous internal oxidation zone (IOZ) immediately under the surface. Further increasing Cr content to 25%, the morphology of reaction products remained basically the same as that of Fe-20Cr, but the surface was rather smooth (Fig. 5c) and the IOZ became thicker (Fig. 5d). The EDS line scan passing through the IOZ Fig. 5e, f confirmed the presence of oxygen in this zone. There were also some metal rich particles appeared inside the IOZ close to the surface (Fig. 5e).

For austenitic alloys, in principle, a uniform attack was observed on the surface after reaction with a thin carburization zone under the surface (Fig. 6a, b and (c)). The typical carbide morphology below alloy surface is shown in Fig. 6d), taking Fe-20Cr-20Ni as an example. A line scan passing through the coke layer

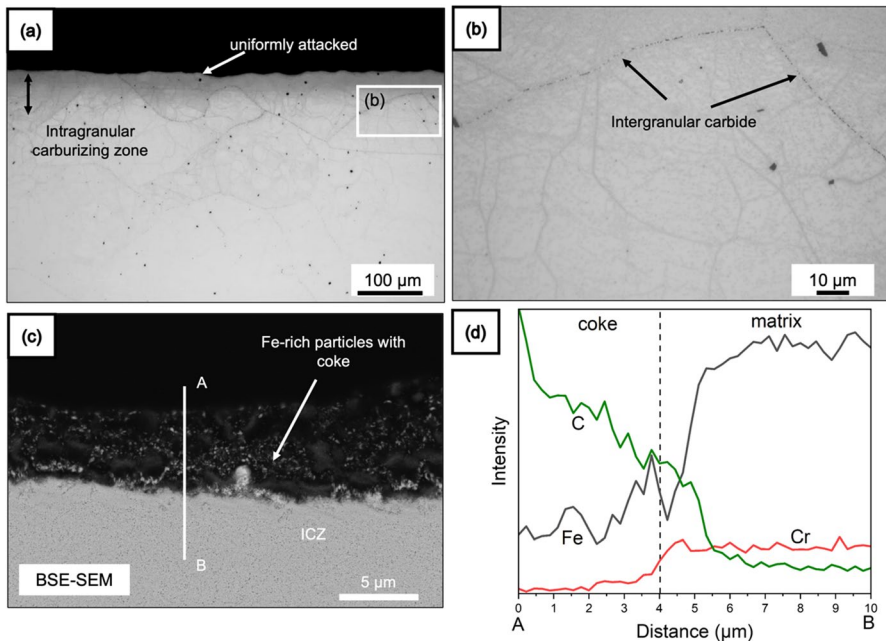


Fig. 4 Metallographic cross sections of **a** Fe-10Cr after 100 h reaction at 550 °C and **b** the region marked in (a); **c** BSE-SEM image of alloy with remaining coke and **(d)** EDS line-scan analysis from A-B in (c)

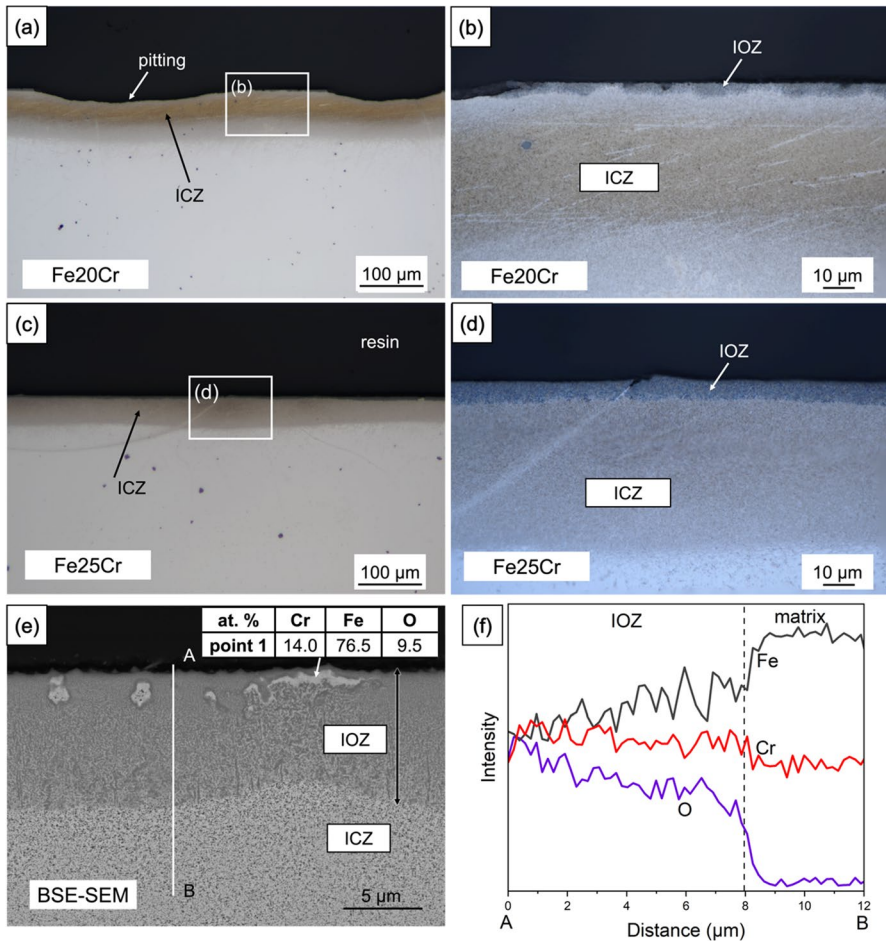


Fig. 5 Metallographic cross sections of **(a, b)** Fe-20Cr and **(c, d)** Fe-25Cr after 100 h reaction at 550 °C **(c)** and **(d)** enlarged areas in **(a)** and **(b)**, respectively); **e** BSE-SEM image of Fe-25Cr with **(f)** EDS line-scan analysis from A-B in **(e)**

and part of carburizing zone for Fe-20Cr-20Ni is shown in Fig. 6e where both Fe and Ni were found with very high C content in the coke layer.

Pitting depths were measured as a distance from the top surface of the thin IOZ (defined as an original metal surface shown in Fig. 5b) to the bottom of the pit. The pitting depths were found to be varied with alloys, as presented in Fig. 7. For Fe-25Cr alloy, the surface was relatively smooth, thus no pitting depth for Fe-25Cr was measured. Fe-20Cr-33Ni was also excluded in Fig. 7 since it had no reference point available. The comparison of pitting depths shown in Fig. 7 indicates a higher Cr content leads to a lower pitting depth, and austenitic alloys have larger pitting depths than ferritic alloys with the same Cr content.

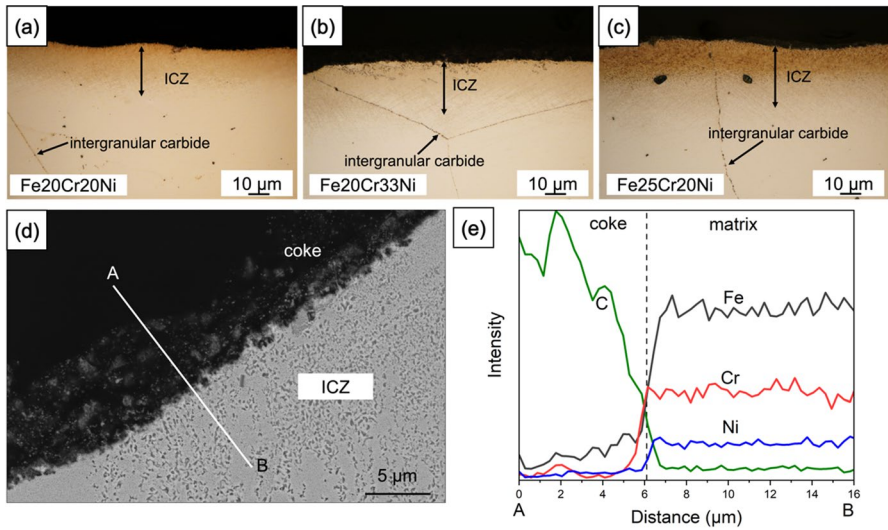


Fig. 6 Metallographic cross sections of **a** Fe-20Cr-20Ni, **b** Fe-20Cr-33Ni and **c** Fe-25Cr-20Ni after 100 h reaction at 550 °C with **d** BSE-SEM image of Fe-20Cr-20Ni and **e** EDS line-scan analysis from A-B in (d)

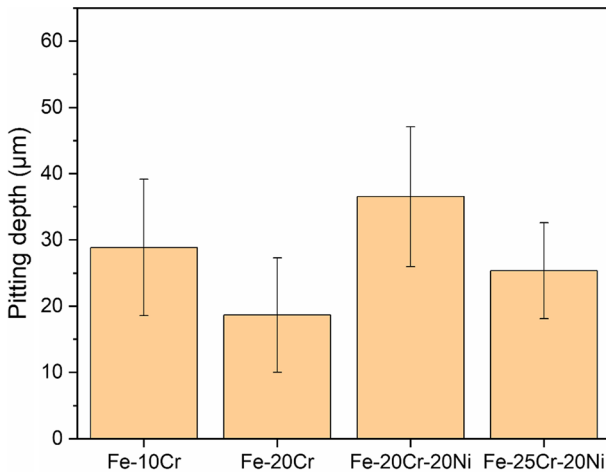


Fig. 7 Pitting depths of some alloys at 550 °C after 100 h reaction

Intragranular carbide precipitation depths were also measured for all alloys and are summarized in Fig. 8 In general, ferritic alloys have higher intragranular carbide depths than those of austenitic alloys. Increasing Cr content reduces carbide depth. Moreover, an intergranular carbide precipitation depth was revealed to be much larger than that of an intragranular carbide precipitation according to measured results of Fe-20Cr-33Ni (intergranular: 141 μm, intragranular: 22 μm).

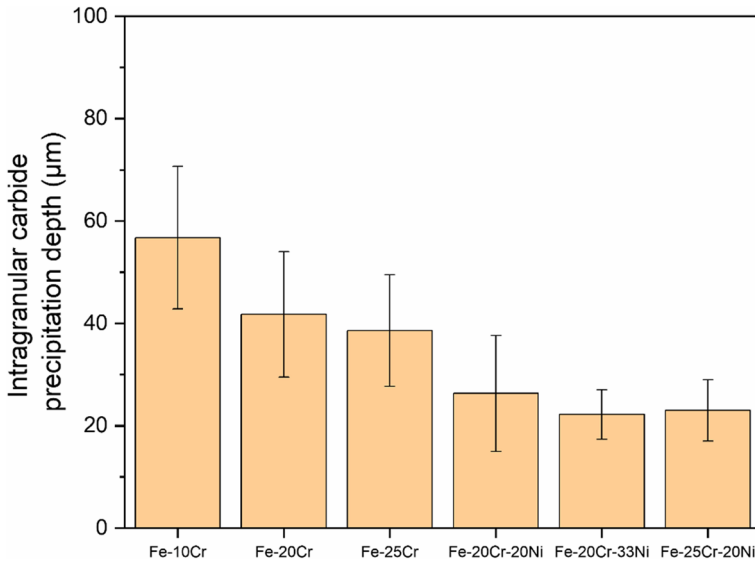


Fig. 8 Intragranular carbide precipitation depths of model alloys at 550 °C after 100 h reaction

This intergranular carbide depth, however, cannot be measured precisely for all alloys because of limited observable grain boundaries.

Reaction at 650 °C

Figure 9a and b present sample weight changes after removing coke and that of coke deposits obtained from coke removal at 650 °C, respectively. All types of alloys except for Fe-20Cr experienced continuous weight gains as time increased, which is different from the results at 550 °C. Fe-10Cr exhibited the highest mass-gain,

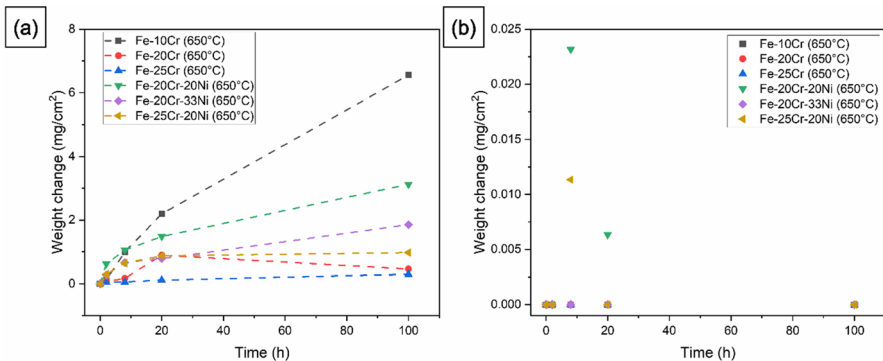
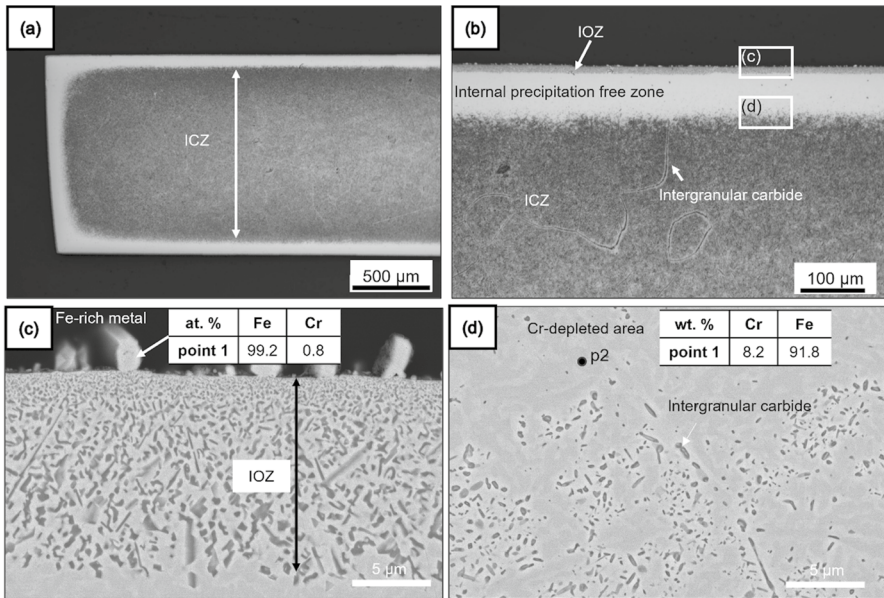


Fig. 9 Weight change kinetics ($\Delta W/A_0$, ΔW : weight change, A_0 : original surface area) at 650 °C **a** samples after removing coke; **b** coke deposits obtained from coke removal

Table 4 Sample surface XRD results after coke removal on the surface at 650 °C

Alloy	Phases
Fe-10Cr	Ferrite, FeCr_2O_4 , Fe_3O_4
Fe-20Cr	Ferrite, Cr_7C_3 , Cr_2O_3 , FeCr_2O_4
Fe-25Cr	Ferrite, Cr_7C_3 , Cr_2O_3 , FeCr_2O_4
Fe-20Cr-20Ni	Austenite, Graphite, Cr_7C_3 , FeCr_2O_4
Fe-20Cr-33Ni	Austenite, Cr_7C_3 , FeCr_2O_4
Fe-25Cr-20Ni	Austenite, Fe_3C , Cr_7C_3 , FeCr_2O_4

**Fig. 10** Metallographic cross sections of Fe-10Cr **a** overview and **b** subsurface area after 100 h at 650 °C; BSE-SEM images of **c** internal oxidation zone and **d** Cr-depleted precipitate-free zone above ICZ as marked in **(b)**

whereas Fe-25Cr showed the least mass-gain. In terms of coke deposits seen in Fig. 9b, almost no coke deposits was obtained although there were couple of very scattered points measured. Unlike at 550 °C, no significant coke formation was observed at 650 °C.

Table 4 shows XRD results of alloys after 100 h reaction at 650 °C. A matrix phase was always identified in all alloys. Graphite and cementite were detected in only Fe-20Cr-20Ni and Fe-25Cr-20Ni, respectively, while Cr_7C_3 was detected in all alloys except for Fe-10Cr. FeCr_2O_4 was identified in all alloys, whereas Cr_2O_3 was only identified in Fe-(20, 25)Cr alloys. Fe_3O_4 was only detected in Fe-10Cr.

Cross sections of post-tested alloys at 650 °C after 100 h reaction were analyzed by optical microscopy, SEM and EDS shown in Figs 10, 11 and 12. In general, no

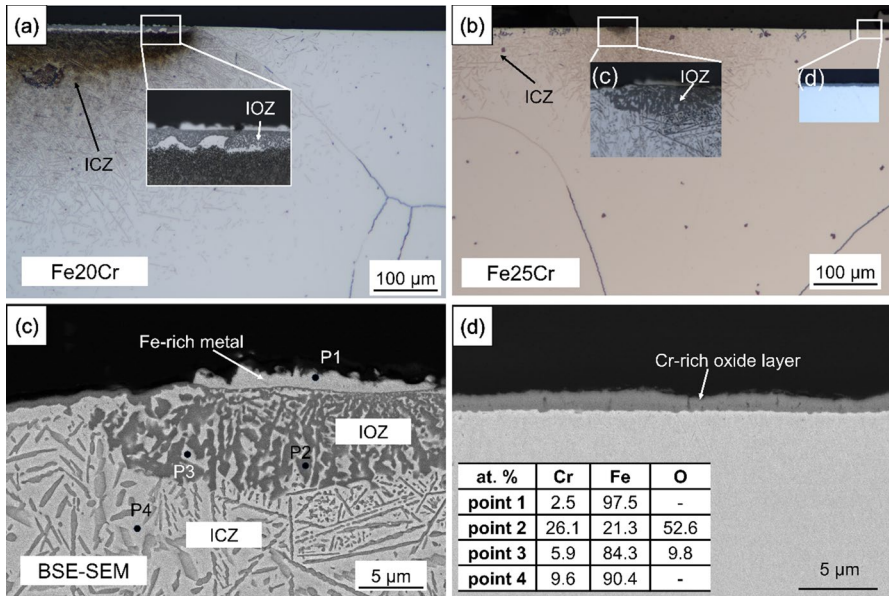


Fig. 11 Metallographic cross sections of **a** Fe-20Cr and **b** Fe-25Cr after 100 h at 650 °C with **c** BSE-SEM images of the Fe-25Cr subsurface region and **(d)** thin Cr-rich oxide layer as indicated in **(b)**

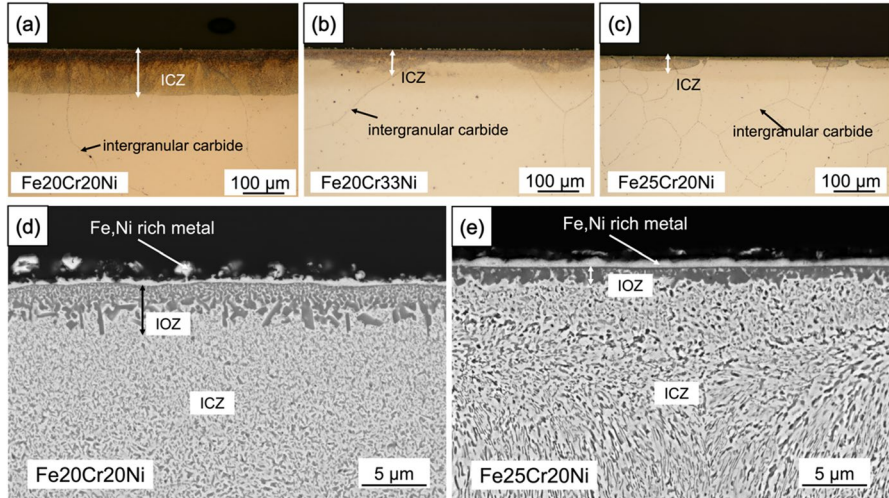


Fig. 12 Metallographic cross sections of **a** Fe-20Cr-20Ni, **b** Fe-20Cr-33Ni and **c** Fe-25Cr-20Ni after 100 h reaction at 650 °C with BSE-SEM images of **d** Fe-20Cr-20Ni and **e** Fe-25Cr-20Ni

pitting but uniform corrosion attack was observed with IOZ and internal carbide precipitates formation in all alloys. For Fe-10Cr, internal carburization zone covered the whole cross section which was surrounded by an internal precipitate free

zone under a thin IOZ near the surface (Fig. 10a, b). High magnification of IOZ in Fig. 10c revealed some Fe-rich nodules formed at the top surface of the IOZ. An EDS point analysis confirmed a lower Cr content in the internal precipitate free zone (Fig. 10d). Increasing Cr concentration reduced the extent of carburization. A predominant thin scale with locally carburized zone formed on Fe-20Cr and Fe-25Cr alloys (Fig. 11a, b). The IOZ could be identified in some local areas of internal carburizing zone, as shown in Fig. 11c. In the carbide-free area, a thin Cr-rich protective oxide scale was formed (Fig. 11d).

For austenitic Fe-20Cr-20Ni, a uniform carburization zone was observed (Fig. 12a). High magnification image revealed the presence of a thin Fe–Ni rich metal layer on the top of the surface, followed by Cr-rich IOZ and then a thick carburizing zone. Further increasing Ni to 33% or Cr to 25%, led to the formation of a nonuniform carburization zone with the reduced thickness (Fig. 12b and c). However, the constitution and the morphologies of corrosion products remained no change, i.e., thin metal layer on the top, the IOZ and thick carburizing zone inside the metal. The morphologies of carbides in the carburizing zone changed with the fine particulate structure near the surface but elongated network structure near the matrix (Fig. 12d, e).

Intragranular carbide precipitation depths are summarized in Fig. 13 where Fe-10Cr is excluded because its carbide precipitation had reached to the center of the cross section (Fig. 10a). In general, ferritic alloys have larger intragranular carbide precipitation depths than those of austenitic alloys with the same Cr concentration, in a similar way as that at 550 °C. In addition, by comparing the thickness of carburizing zone at 550 and 650 °C (Figs. 8 and 13), the thicknesses of carburizing zone increased at higher temperature.

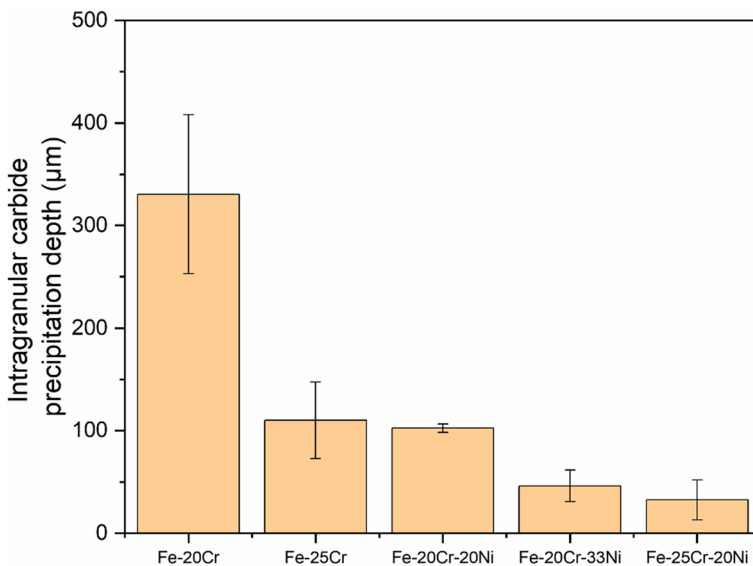


Fig. 13 Intragranular carbide precipitation depths of some model alloys at 650 °C after 100 h reaction

As for IOZ growth, it was revealed to follow a parabolic rate law using a linear fit of IOZ thickness vs $t^{1/2}$ (Fe-10Cr in Fig. 14). All other alloys had only two sets of data and therefore no linear plots were given. The IOZ thickness after 100 h reaction at 650 °C is shown in Fig. 15. Again, ferritic alloys had higher IOZ than austenitic alloys and increasing Cr concentration reduced the IOZ thickness.

Discussion

All alloys except Fe-25Cr at 550 °C had undergone mass loss with coke deposits after 100 h reaction (Fig. 3a, b), and the results of XRD analysis revealed the presence of graphite and carbides in the products (Table 3). Additionally, Fe-rich particles were observed in cross sections of coke deposits (Figs. 4 and 6). These results indicate metal dusting had occurred, leading to extensive mass losses (Fig. 3a). In contrast, Fe-25Cr at 550 °C was found to have no significant mass loss, presenting a higher resistance to metal dusting than other alloys (Fig. 3a). On the other hand, all alloys at 650 °C received weight gains without a significant coke deposition, although the calculated gas carbon activity was greater than unity. Cross-sectional observations at 650 °C revealed the dominant internal precipitation of oxides and carbides, contributing to mass gains. However, Fe-(20, 25)Cr exhibited no significant mass gain, which would be the impact of an external discontinued Cr-rich oxide layer (Fig. 11) on reducing internal oxide and carbide precipitation.

Internal oxides and carbides were also found in alloys at 550 °C according to cross-sectional observations (Figs. 4, 5 and 6), but no mass gain was seen after the

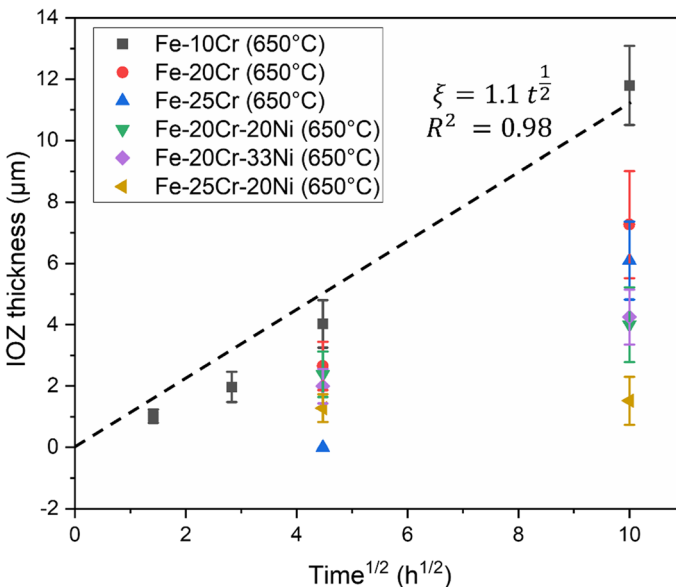


Fig. 14 IOZ thickness of alloys as a function of square root of time at 650 °C

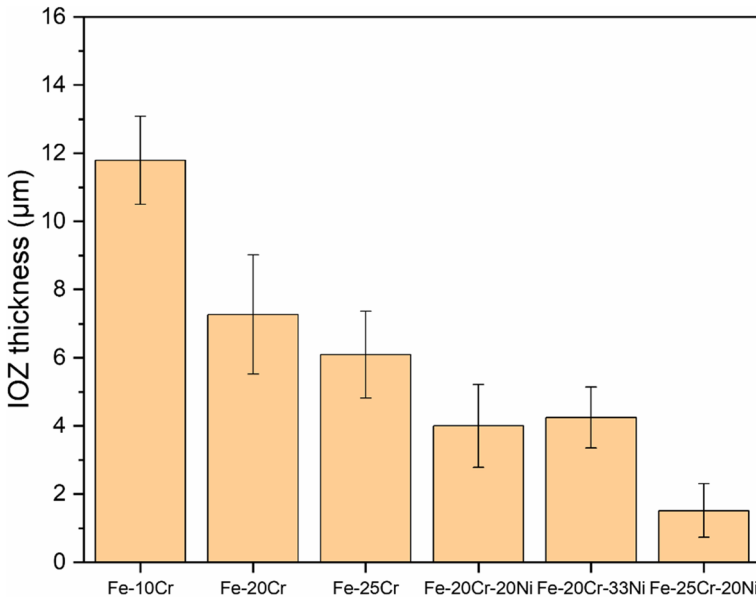


Fig. 15 IOZ thickness of model alloys at 650 °C after 100 h reaction

coke removal. This indicates that the mass loss due to metal dusting was larger than the mass gain due to the formation of oxides and carbides after 100 h. However, all types of alloys at 550 °C after 20 h except for Fe-10Cr had undergone a mass gain (Fig. 3a), indicating the mass gains at the early stage due to internal oxide and carbide precipitation were predominant. Therefore, mass change kinetics reflect not only metal dusting but also internal oxidation and carburization. As shown in this work, these kinetics depended on many factors, including alloy composition and reaction temperature which will be discussed separately.

Metal Dusting

It is known that Cr addition into an alloy can retard the onset of metal dusting by forming a protective Cr oxide layer on the surface and forming internally Cr carbides prior to a graphite nucleation/formation [5, 8, 9, 15]. Therefore, increasing Cr content will increase the protection of alloy, which is true as shown in Fig. 7 where a reduced pitting depth is shown for both ferritic and austenitic alloys with increased Cr contents. As Cr diffusivity in an austenitic alloy is slower than that in a ferritic alloy [5], it is reasonable that a slower diffusion of Cr in austenite could delay the formation of chromia and therefore less protective than the ferrite with the same Cr content which is in line with the observation of higher pitting depth of Fe-20Cr-20Ni than that of Fe-20Cr.

Metal dusting is known to take place accompanying with graphite nucleation, and it requires supersaturation of the dissolved carbon in the matrix. The degree

of carbon supersaturation required for graphite nucleation is generally reported to be higher than that for forming carbides [20]. In this study, the calculated gas carbon activity based on the Boudouard reaction at 650 °C is much greater than unity, while that based on hydrogenation reaction is only around unity. The observed no carbon deposition at 650 °C indicates that the Boudouard reaction does not play a key role in carbon deposition, which is in line with the reports that carbon production from the Boudouard reaction is much slower than that from the hydrogenation reaction [20]. Therefore, it is reasonable to conclude that carbon deposition is controlled mainly by the hydrogenation reaction. An actual gas carbon activity would be locally varied due to non-equilibrium state during reaction, indicating the gas carbon activity based on hydrogenation reaction might be below one in the actual condition. Thus, no significant coke deposition and metal dusting were observed at 650 °C because of an insufficient degree of carbon supersaturation from the hydrogenation reaction although the calculated carbon activity exceeds unity. At a lower temperature of 550 °C, carbon activity of reaction gas increases significantly in both the hydrogenation reaction and the Boudouard reaction. The observed carbon deposition and coke formation indicate that the carbon activity at this temperature is well above the critical value for carbon deposition and metal dusting formation.

Carburization

Internal carbide formation was seen for all alloys at both temperatures. According to Figs. 8 and 13, a higher temperature led to a greater carbide precipitation depth. The carbon diffusion coefficient, D_C , for example, for Fe–Ni austenitic alloy at 500–900 °C as a function of temperature can be expressed as follows [21]:

$$D_C = 1.23 \times 10^{-6} e^{-\frac{15050}{T}} \left(\text{m}^2/\text{s} \right) \quad (4)$$

where T is temperature in Kelvin. In addition, it is acknowledged the carburizing depth, ξ_C , in alloys and thickening rate constant, k_p can be expressed [22], respectively:

$$\xi_C = [2k_p t]^{\frac{1}{2}} \quad (5)$$

$$k_p = \frac{\varepsilon D_C N_c}{\nu N_M} \quad (6)$$

where N_c is the carbon solubility, N_M is the mole fraction of elements such as Cr for forming carbides in the alloy, ν is the stoichiometric ratio for the carbides, and ε is a labyrinth factor to consider the diffusional blocking effect of the precipitates. From Eqs. 5 and 6, a carbide precipitation depth, ξ_C , can be described as a function of square root of a carbon diffusion coefficient if assuming carbon solubility is the same. Square root of carbon diffusion coefficients at 550 and 650 °C calculated by Eq. 4 are shown in Table 5. The ratio of measured intragranular carbide precipitation depth of Fe-20Cr-33Ni at 650 °C to that of same alloy at 550 °C after 100 h

Table 5 Calculated carbon diffusion coefficient in Fe–Ni alloy at 550 and 650 °C

Temperature (°C)	Carbon diffusion coefficient	
	D (m ² /s)	\sqrt{D}
550	1.41×10^{-14}	1.12×10^{-7}
650	1.02×10^{-13}	3.19×10^{-7}

reaction is 2.1. Meanwhile, the calculated ratio of \sqrt{D} at two temperatures is 2.7 which is very close to the measured ratio, indicating that the different intragranular carbide precipitation depths between 550 °C and 650 °C is largely attributed to the variation in carbon diffusion coefficient at these temperatures.

From Figs. 8 and 13, the higher Cr content was found to lead to smaller intragranular carbide precipitation depth in both ferritic and austenitic alloys at both temperatures. This is consistent with [22] and can be well explained by Eqs. 5 and 6 where increasing Cr content reduces k_p and therefore the carburizing depth. Measured volume fractions of intragranular carbides in carburizing zones at 550 °C are shown in Table 6, indicating a higher Cr content alloy has a larger volume fraction of intragranular carbide precipitates, leading to its smaller carbide precipitation depth due to a slower carbon diffusion in the denser carburizing zone.

For austenitic alloys, Fe-(20, 25)Cr-20Ni have very similar volume fractions of intragranular carbides (Table 6). Moreover, smaller depths of carbide precipitates were found in austenitic alloys than that in ferritic alloys with the same Cr concentration at both temperatures, as shown in Figs. 8 and 13. This is in agreement with a lower carbon permeability in austenitic alloys than that in ferritic alloys [23]. The higher depth of carbide precipitates on Fe-20Cr-20Ni than that on Fe-20Cr-33Ni at both temperatures can be explained by the reduced carbon permeability with increasing the Ni content [5].

Oxidation

External Cr₂O₃ layer and internal Cr-rich oxide precipitates were found in some cross-sectional observations. An external Cr₂O₃ layer was clearly seen in Fe-20Cr and Fe-25Cr at 650 °C (Fig. 11), whereas it was not seen in Fe-10Cr (Fig. 10) and austenitic alloys at 650 °C (Fig. 12). Additionally, no external Cr₂O₃ layer was observed in Fe-20Cr and Fe-25Cr at 550 °C (Fig. 5). These findings indicate that

Table 6 Average volume fraction of intragranular carbide precipitates in carburizing zone at 550 °C after 100 h reaction

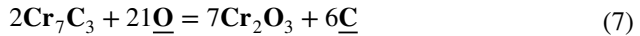
Alloy	Average volume fraction of intragranular carbides (%)
Fe-10Cr	26.0
Fe-25Cr	41.0
Fe-20Cr-20Ni	42.1
Fe-25Cr-20Ni	42.6

at a higher temperature, a ferritic alloy leads to a lower critical Cr concentration to form the external Cr_2O_3 layer. The critical concentration, N_{Cr} , above which the oxide scale transfers from the internal oxidation to the external oxidation can be calculated using the following equation:

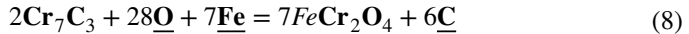
$$N_{\text{Cr}} = \left(\frac{\pi g^*}{2\nu} N_{\text{O}}^{(S)} \frac{D_{\text{O}} V_{\text{m}}}{\bar{D}_{\text{Cr}} V_{\text{CrOv}}} \right)^{\frac{1}{2}} \quad (7)$$

where g^* is the critical volume fraction of oxide from internal to external oxidation (usually 0.3 [24]), and ν is the stoichiometric coefficient of oxide CrOv . $N_{\text{O}}^{(S)} D_{\text{O}}$ represents oxygen permeability, \bar{D}_{Cr} is chromium inter-diffusion coefficient, and V_{m} and V_{CrOv} are the mole volume of alloy and oxide, respectively. Increasing temperature significantly increases \bar{D}_{Cr} and therefore reduces N_{Cr} . Similarly, at the same temperature, \bar{D}_{Cr} is much higher for ferrite than that for austenite, leading to the accelerated chromia formation [5]. Although both temperature and steel structure also affect oxygen permeability, this affection is in general less significant than that on Cr diffusion [25].

Internal Cr_2O_3 precipitation, forming an IOZ, was found to be located close to the surface and immediately above the internal carburizing zone (Figs. 5, 10–12). This phenomenon has been reported by many researchers and is attributed to the conversion of the carbides to more stable oxides near the alloy surface with a lower Cr activity and a higher oxygen potential environment [4, 20, 26]. The reactions are as follows:



or



The removed carbon from Reaction 7 and/or 8, then, diffuses into the deeper matrix, and reacts with metal to form carbides. Thus, internal carbide precipitates were seen below IOZ, in line with the previous studies [20, 26].

Metal nodules, observed on the surface immediately above IOZ in this study (Figs. 10c, 11c, and 12d, e), are attributed to the volume expansion due to internal oxide formation which expels matrix metal to the surface. Similar observation was reported extensively in different Ni-based alloy systems with IOZ formation [27–29].

IOZ thicknesses at 650 °C shown in Figs. 14 and 15 illustrate that the IOZ thickness reduces with increasing Cr concentration in the alloy. This is consistent with the relationship between the internal oxide precipitation depth, ξ_{O} and the initial Cr concentration in the alloy, N_{Cr}^{O} , expressed as follows [22]:

$$\xi_{\text{O}} = \left[\frac{2N_{\text{O}}^{\text{S}} D_{\text{O}}}{\nu N_{\text{Cr}}^{\text{O}}} t \right]^{\frac{1}{2}} \quad (9)$$

where N_{O}^{S} is the oxygen solubility, D_{O} is the oxygen diffusivity in the alloy, and ν is the stoichiometric coefficient of oxide CrO_ν . Measured volume fractions of internal

Table 7 Average volume fraction of internal oxide precipitates in IOZ

Alloy	Average volume fraction of internal oxide precipitates (%)
Fe-10Cr	36.0
Fe-25Cr	70.2
Fe-20Cr-20Ni	65.4
Fe-25Cr-20Ni	71.4

oxide precipitates in IOZ are summarized in Table 7, indicating a higher Cr content alloy contains a larger volume fraction of internal oxides in the IOZ in both ferritic and austenitic alloys. This implies that a larger volume fraction of internal oxides would cause a slower oxygen diffusion, resulting in a reduced thickening kinetics of IOZ.

Additionally, ferritic alloys form thicker IOZs than austenitic alloys at 650 °C (Fig. 15), which can be attributed to a higher oxygen permeability in ferrite than that in austenite [26]. Under this basis, it is expected that increasing Ni concentration in the austenitic alloy could reduce the IOZ because of the lowered oxygen permeability [24]. However, this decrease in IOZ thickness was not observed by comparing the results of Fe-20Cr-20Ni and Fe-20Cr-33Ni in Fig. 15. This phenomenon could be explained as follows. The impact of Ni addition on lowering the oxygen permeability was found to be greater at 1150 °C than that at 1100 °C [24], indicating a higher temperature would cause a greater contribution of Ni concentration to lower the oxygen permeability. Thus, relatively lower temperature conditions in this study possibly led to no significant effect of Ni addition on oxygen permeability and therefore, IOZ kinetics.

As mentioned in introduction, this study only reveals the early stage of metal dusting of model alloys under a simulated blast furnace operating condition. Although these short-term experiments provide some useful information for understanding the initial stage of metal dusting in the blast furnace gas condition, long-term gas exposure experiments are necessary to evaluate the propagation of metal dusting for industrial applications which should be done in future.

Another factor affecting metal dusting in the blast furnace ironmaking is the varied temperature in a real blast furnace operating condition. Reaction tests in this study were carried out at an isothermal condition, while temperature in a blast furnace varied with each operating stage. Such a varied temperature condition has been reported to cause damage and spallation of a protective oxide scale on the alloy surface, accelerating the occurrence of metal dusting from the Cr-depleted region. Thus, consideration of temperature variation including temperature range and cyclic rate is needed to investigate corrosion behavior under blast furnace operating conditions.

Unlike other reaction conditions commonly used for metal dusting research with much higher carbon activities, this low carbon activity blast furnace gas is potential to form metal dusting as revealed in this work at relatively lower temperatures, e.g.,

550 °C, but becomes marginal at higher temperatures, e.g., at 650 °C. Carbon activity should still be an important factor to control the occurrence of metal dusting.

Conclusions

In this study, several model alloys: Fe-(10, 20, 25)Cr, Fe-20Cr-(20, 33)Ni, and Fe-25Cr-20Ni alloys with electropolished surfaces were tested in the gas mixture of Ar-33CO-7H₂-7CO₂-2H₂O at 550 °C and 650 °C up to 100 h. The gas mixture was simulated to an environment in a blast furnace, containing relatively lower level of hydrogen and other gas components, which was rarely investigated by early studies. It was found that temperature and alloy compositions highly affected alloy corrosion behaviors and kinetics.

At 550 °C, severe metal dusting was found for all alloys except Fe-25Cr which showed no significant metal dusting. At 650 °C, however, no significant coke deposition and metal dusting were seen, but extensive carburization and oxidation occurred. This phenomenon was attributed to the relatively slower rate of carbon production but higher reaction kinetics of oxidation and carburization at 650 °C than at 550 °C. In addition, the formation of a thin matrix metal layer at the top surface of IOZ was found at 650 °C, which was attributed to the volume expansion due to the internal oxide formation which expels metal to the surface. Forming an external Cr₂O₃ layer was clearly found to be beneficial for protecting alloys from coke deposition, metal dusting, and carburization, and a higher temperature condition was revealed to lead to a reduced critical Cr concentration for forming adherent Cr-rich oxide layer.

Alloy compositions of Cr and Ni are important to affect corrosion behaviors at both temperatures. At 550 °C, increasing Cr concentration for ferritic Fe–Cr alloys and Cr and/or Ni concentrations for austenitic Fe–Ni–Cr alloys were found to reduce the kinetics of coke deposition, metal dusting, and carburization. At 650 °C, reduced kinetics of carburization and IOZ thickness were found with increasing Cr content in both ferritic and austenitic alloys. However, increasing Ni content in austenitic alloys only reduced kinetics of carburization.

In terms of impacts of alloy structure, it was revealed that with the same Cr concentration, a ferritic alloy showed a higher resistance to metal dusting than an austenitic alloy, although the ferritic alloy was more susceptible to carburization at 550 °C. At 650 °C, a ferritic alloy experienced higher extents of carburization and oxidation than an austenitic alloy with the same Cr concentration.

Acknowledgements Financial support from the Australian Research Council under the Discovery Program is highly appreciated.

Author Contributions Conceptualization: Tatsuya Murakami and Jianqiang Zhang; Methodology: TM, TDN, and JZ; Formal analysis and investigation: Tatsuya Murakami, TDN, and XX; Writing – original draft preparation: TM; Writing – review and editing: XX; JZ; Supervision: JZ.

Funding Open Access funding enabled and organized by CAUL and its Member Institutions.

Data Availability The raw data required to reproduce these findings cannot be shared at this time as the data also form part of ongoing study. The processed data required to reproduce these findings cannot be shared at this time the data form part of an ongoing study.

Declarations

Conflict of interest The authors have no competing interests to disclose that are relevant to this article.

Open Access This article is licensed under a Creative Commons Attribution 4.0 International License, which permits use, sharing, adaptation, distribution and reproduction in any medium or format, as long as you give appropriate credit to the original author(s) and the source, provide a link to the Creative Commons licence, and indicate if changes were made. The images or other third party material in this article are included in the article's Creative Commons licence, unless indicated otherwise in a credit line to the material. If material is not included in the article's Creative Commons licence and your intended use is not permitted by statutory regulation or exceeds the permitted use, you will need to obtain permission directly from the copyright holder. To view a copy of this licence, visit <http://creativecommons.org/licenses/by/4.0/>.

References

1. C. H. Toh, P. R. Munroe, and D. J. Young, Metal Dusting of Fe–Cr and Fe–Ni–Cr Alloys Under Cyclic Conditions. *Oxidation of Metals* **58**, (1), 2002 (1–21).
2. C. H. Toh, P. R. Munroe, and D. J. Young, *Materials at High Temperatures* **20**, (4), 2003 (527–534).
3. Z. Zeng and K. Natesan, *Oxidation of Metals* **66**, (1), 2006 (1–20).
4. D. J. Young, J. Zhang, C. Geers, and M. Schütze, *Materials and Corrosion* **62**, (1), 2011 (7–28).
5. H. J. Grabke and M. Spiegel, *Materials and Corrosion* **54**, (10), 2003 (799–804).
6. Y. Nishiyama, T. Kudo, and N. Otsuka, *CORROSION* **62**, (1), 2006 (54–63).
7. J. Orlikowski, A. Jazdzewski, K. Darowicki, J. Karczewski, and J. Dampc, *Engineering Failure Analysis* **91**, 2018 (108–114).
8. S. Strauß and H. J. Grabke, *Materials and Corrosion* **49**, (5), 1998 (321–327).
9. H. J. Grabke, E. M. Müller-Lorenz, and H. P. Martinz, *Materials and Corrosion* **54**, (11), 2003 (860–863).
10. K. Nakano, Y. Ujisawa, T. Inada, A. Oboso, and K. Katayama, *Advanced Technologies for Blast Furnace Life Extension*. 2020, Nippon steel. p. 109–118.
11. A. M. Heikkilä, A. M. Koskela, M. O. Iljana, R. Lin, H. Bartusch, E.-P. Heikkinen, and T. M. J. Fabritius, *Steel research international* **92**, (3), 2021 (e2000456).
12. Z. Zhang, J. Meng, L. Guo, and Z. Guo, *JOM* **67**, (9), 2015 (1936–1944).
13. X. F. Dong, A. B. Yu, S. J. Chew, and P. Zulli, *Metallurgical and Materials Transactions B* **41**, (2), 2010 (330–349).
14. T. Yamamoto, T. Sato, H. Fujimoto, T. Anyashiki, K. Fukada, M. Sato, K. Takeda, and T. Ariyama, *Tetsu-to-Hagane* **97**, (10), 2011 (501–509).
15. L. Melo-Máximo, M. Pérez, J. Lin, O. Salas, D. Melo-Máximo, J. Oseguera, V. M. López-Hirata, R. D. Torres, and R. M. Souza, *Surface Engineering* **31**, (2), 2015 (166–172).
16. G. Palasantzas, H. J. Kooij, and J. T. M. DeHosson, *Applied Surface Science* **229**, (1), 2004 (190–196).
17. W.M. Haynes, *CRC handbook of chemistry and physics, 95th Edition*. 95th ed. Handbook of chemistry and physics. 2014, Hoboken: CRC Press.
18. C. W. Bale, E. Béglise, P. Chartrand, S. A. Decterov, G. Eriksson, A. E. Gheribi, K. Hack, I. H. Jung, Y. B. Kang, J. Melançon, A. D. Pelton, S. Petersen, C. Robelin, J. Sangster, P. Spencer, and M. A. Van Ende, *Calphad* **54**, 2016 (35–53).
19. C. A. Schneider, W. S. Rasband, and K. W. Eliceiri, *Nature Methods* **9**, (7), 2012 (671–675).
20. J. Zhang, K. Boddington, and D. J. Young, *Corrosion Science* **50**, (11), 2008 (3107–3115).
21. P. Thibaux, A. Métenier, and C. Xhoffer, *Metallurgical and Materials Transactions A* **38**, (6), 2007 (1169–1176).
22. C. Wagner, *Zeit. Elektrochem.* **63**, (7), 1959 (772–782).

23. C.H. Toh, *Metal dusting on heat-resistant alloys under thermal cyclic conditions*, in *School of Materials Science and Engineering*. 2002, University of New South Wales.
24. D. Jullian, A. Prillieux, J. Zhang, and D. J. Young, *Materials and Corrosion* **68**, (2), 2017 (197–204).
25. K. K. Aye, Y. Cai, J. Zhang, and D. J. Young, *Oxidation of Metals* **97**, (3), 2022 (371–400).
26. M. Hänsel, C. A. Boddington, and D. J. Young, *Corrosion Science* **45**, (5), 2003 (967–981).
27. C. Jiang, Y. Xie, C. Kong, J. Zhang, and D. J. Young, *Corrosion Science* **174**, 2020 108801.
28. H. C. Yi, S. W. Guan, W. W. Smeltzer, and A. Petric, *Acta Metallurgica et Materialia* **42**, (3), 1994 (981–990).
29. G. C. Wood, F. H. Stott, D. P. Whittle, Y. Shida, and B. D. Bastow, *Corrosion Science* **23**, (1), 1983 (9–25).

Publisher's Note Springer Nature remains neutral with regard to jurisdictional claims in published maps and institutional affiliations.